

Three-layer deep learning network random trees for fault diagnosis in chemical production process

Ming Lu, Zhen Gao, Ying Zou, Zuguo Chen, Pei Li

School of Information and Electrical Engineering, Hunan University of Science and Technology, Xiangtan, China

Correspondence

Zhen Gao, School of Information and Electrical Engineering, Hunan University of Science and Technology, Xiangtan, China.

Email: Z.Gao@mail.hnust.edu.cn

Funding information

National Natural Science Foundation of China, Grant/Award Numbers: 62203164, 62373144; Scientific Research Fund of Hunan Provincial Education Department (Outstanding Young Project), Grant/Award Number: 21B0499; Hunan Provincial Department of Education, Grant/Award Number: 22A0349

Abstract

With the development of technology, the chemical production process is becoming increasingly complex and large-scale, making fault diagnosis particularly important. However, current diagnostic methods struggle to address the complexities of large-scale production processes. In this paper, we integrate the strengths of deep learning and machine learning technologies, combining the advantages of bidirectional long and short-term memory neural networks, fully connected neural networks, and the extra trees algorithm to propose a novel fault diagnostic model named three-layer deep learning network random trees (TDLN-trees). First, the deep learning component extracts temporal features from industrial data, combining and transforming them into a higher-level data representation. Second, the machine learning component processes and classifies the features extracted in the first step. An experimental analysis based on the Tennessee Eastman process verifies the superiority of the proposed method.

KEYWORDS

chemical production, process monitoring, fault diagnosis, TDLN-trees, Tennessee Eastman

1 INTRODUCTION

In the rapidly developing chemical production field, the emergence of intelligent control systems presents new opportunities and challenges^[1]. The control system can intelligently schedule and utilize resources to maximize production efficiency. However, the complex processes and harsh operating conditions in chemical production expose control systems to risks like toxic corrosion and safety management challenges^[2]. Interdependence of system components means that failure of any component can cause cascading failures, leading to serious property damage^[3]. This risk is compounded by the production process's instability. These issues underline the urgent need for intelligent and effective fault detection and diagnosis (FDD) methods in the chemical industry to make the production process more flexible and controllable^[4,5].

The development and refinement of FDD methods have long been a key research focus. Traditional FDD methods include nonlinear observer-based method, filter-based method, differential geometry method, and so on. The nonlinear observer-based method converts the nonlinear fault diagnostic problem into a linear fault diagnostic problem for special nonlinear systems^[6]; the filter-based method generates residuals at the equilibrium point of the system for local linearization for nonlinear discrete systems^[7]; the differential geometry method decomposes the system in state transformations, and designs observers for the decomposed subsystems to realize the detection and separation of faults^[8]. However, with the advent of the big data era, the complex and huge amount of data makes it difficult for these methods to maintain accuracy and timeliness in FDD^[9].

The above shifts have promoted the adoption of FDD methods based on data-driven approaches, which are no longer based on traditional physical models or theoretical knowledge for troubleshooting, but rather on understanding the system behaviour by analyzing large amounts of data^[10]. Data-driven FDD methods include statistical-based methods, machine learning-based methods, and deep learning-based methods. Statistical-based methods such as principal component analysis (PCA) and partial least squares (PLS). Both PCA and PLS belong

to the data dimensionality reduction techniques. PCA simplifies data structure by transforming it into linearly uncorrelated variables through orthogonal transformation^[11]. PLS builds linear regression models between multiple predictor and response variables to elucidate industrial processes^[12]. However, neither can be applied to nonlinear systems. To address this issue, kernel principal component analysis (KPCA) was developed. KPCA is the nonlinear extension of PCA, which maps the original features to a high-dimensional space via the kernel function to make the nonlinear structure linearly separable, and then performs PCA in the space^[13]. KPCA can address the nonlinear challenges in complex industrial processes. However, selecting the suitable KPCA kernel and adjusting its parameters relies on prior experience.

Machine learning-based FDD methods such as the support vector machine (SVM) and random forest algorithm (RF), etc^[14]. SVM is suitable for nonlinear, high-dimensional systems, constructing hyperplanes to separate variable state classes in a multidimensional space for fault diagnosis^[15,16]. However, SVM is a binary classification algorithm, requiring an extension strategy for multiclassification problems, which causes an additional computational load. RF is an integrated learning algorithm, which realizes fault diagnosis by constructing a decision tree with multiple subsets of different features^[17]. RF performs well on multiclassification problems but is not an optimal choice for high-dimensional data or structured data. The Extra Trees algorithm (ET) improves upon RF by introducing greater randomness. Arya M et al. utilized ET to select the best subset of features, which were fed into a deep learning network for early-stage diabetes prediction with an accuracy of over 97%^[18]. S. Yousefi et al. applied ET to machine part fault diagnosis, optimizing ET parameters with the Bayesian optimization method, reaching up to 99% accuracy^[19]. Overall, ET demonstrates robustness with complex data for high-precision fault diagnosis, but its parameters need to be optimized to obtain optimal performance.

As industrial processes become more automated and complex. Deep learning-based FDD methods are becoming the cutting edge of the field^[20]. Deep learning-based FDD methods include autoencoder (AE), convolutional neural network (CNN), and long-short-term memory network (LSTM), etc. AE can learn the compressed representation of input data and reconstruct input data, then determine the occurrence of faults by monitoring the reconstruction errors of fault data^[21]. However, the feature extraction and recognition ability of AE are weaker than

those of some supervised learning algorithms. CNN performs well in the domains with spatial correlation such as image recognition and video analytics, it identifies the fault patterns by learning the spatial hierarchies in the data to realize fault diagnosis^[22]. However, CNN is not good at processing time series data. LSTM, ideal for data with temporal correlations, learns long and short-term dependencies through a gating mechanism to capture anomalous patterns over time^[23]. Zhang S et al. innovatively combined LSTM with a trapezoidal auto-encoder for application to continuous stirred-tank heaters and the Tennessee Eastman Benchmark Process, achieving over 95% fault diagnosis rate^[24]. Because the number of hidden layer nodes in LSTM has impacts on the accuracy of fault diagnosis and the number of iterations to find the optimal solution, Han Y et al. determined the optimal number of LSTM hidden layer nodes for various faults by comparing training errors, resulting in enhanced fault diagnosis accuracy^[25].

To address the above background, we integrate the strengths of deep learning techniques and machine learning techniques, combine the advantages of bidirectional long and short-term memory neural network (BLSTM), LSTM, fully connected neural network (FCNN), and ET, and propose a new fault diagnosis model named three-layer deep learning network random trees (TDLN-trees). TDLN-trees starts with the sliding window method to extract offline samples of industrial process variables, which ensures the temporal integrity and relevance of the data. Next, the fault data are normalized with normal operating state data, and the fault labels are one-hot encoded. In the subsequent training process, TDLN-trees uses the multiple LSTM and FCNN structures in its deep learning component to capture and fit complex features from the time series data, then ET in the machine learning component to realize fault classification. Therefore, in the process of online fault diagnosis, TDLN-trees can use the efficient feature extraction capability of deep learning and the excellent classification capability of machine learning to analyze the online process variables of chemical production and realize fault diagnosis.

The rest of the paper is organized as follows: section 2 reviews the basic theory of BLSTM, LSTM, and ET. Section 3 introduces the data extraction and preprocessing operations required for fault diagnosis by TDLN-trees. Section 4 presents the structural components of TDLN-trees and the fault diagnosis steps. An experimental analysis based on the Tennessee Eastman process

is conducted in Section 5 to validate the effectiveness of TDLN-trees. Finally, Section 6 provides conclusions.

2 PRELIMINARIES

TDLN-trees combine the advantages of algorithms such as LSTM, BLSTM, and ET, and the following is a brief description of these methods:

2.1 LSTM

LSTM is a modified Recurrent Neural Network (RNN) model, as shown in Figure 1(A and B) demonstrates the network structure of RNN and LSTM. LSTM achieves the adaptive memory of important information and accurate forgetting of redundant information by adding three gating structures, namely, the forget gate f , the input gate i , and the output gate o . Moreover, LSTM overcomes the problems of gradient explosion and vanishing that RNNs face when processing complex time series data^[26,27].

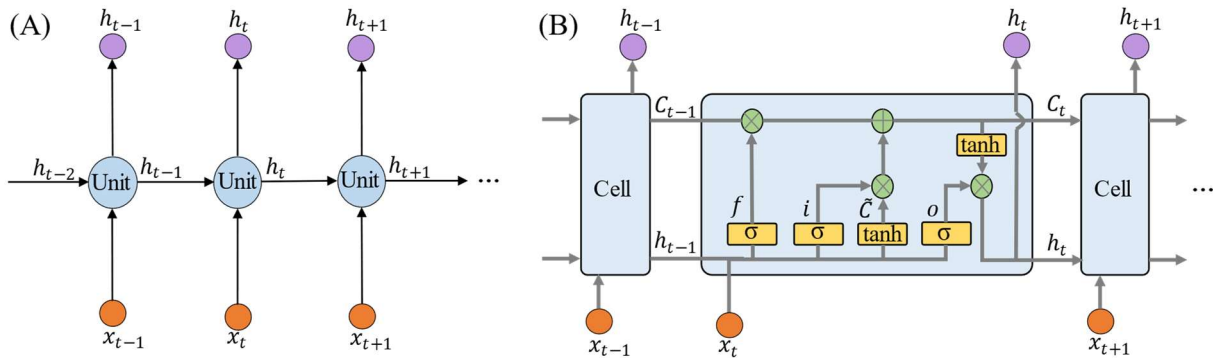


FIGURE 1 The structure of RNN and LSTM.

The forget gate f determines which information from the previous time step is discarded at time t . The value of the forget gate f is denoted as f_t (Equation (1)). The input gate i and its accompanying candidate cell state gate \tilde{C} determine which information will be added to the memory cell at time t , denoting the values of the input gate i and the candidate cell state gate \tilde{C} as i_t and \tilde{C}_t (Equations (2) and (3)), respectively. The updated value C_t of the memory cell at time t is based on the forget gate, the input gate, and the candidate state gate (Equation (4)). The output gate o determines which information is output by this memory cell at time t , the

value of the output gate o is denoted as o_t (Equation (5)), and the output of the memory cell is denoted as h_t (Equation (6)). At the initial time ($t = 0$), i_t , C_t , and o_t are typically set to a value close to 0, while f_t is usually initialized to a value close to 1. The state values of each gate at time t are as follows:

$$f_t = \sigma(W_f \cdot [x_t, h_{t-1}] + b_f) \quad (1)$$

$$i_t = \sigma(W_i \cdot [x_t, h_{t-1}] + b_i) \quad (2)$$

$$\widetilde{C}_t = \tanh(W_C \cdot [x_t, h_{t-1}] + b_C) \quad (3)$$

$$C_t = f_t * C_{t-1} + i_t * \widetilde{C}_t \quad (4)$$

$$o_t = \sigma(W_o \cdot [x_t, h_{t-1}] + b_o) \quad (5)$$

$$h_t = o_t * \tanh(C_t) \quad (6)$$

As time goes on, the feature information of the data passes sequentially through the memory cells and is added to or deleted from the memory cells through gate structures, enabling LSTM to process time-series data effectively.

2.2 BLSTM

BLSTM, developed from LSTM, introduces the concepts of forward and reverse temporal directions, allowing the network to consider both past and future information of the input data sequence. BLSTM captures the before-and-after temporal relationships more comprehensively^[28]. Its structure is shown in Figure 2.

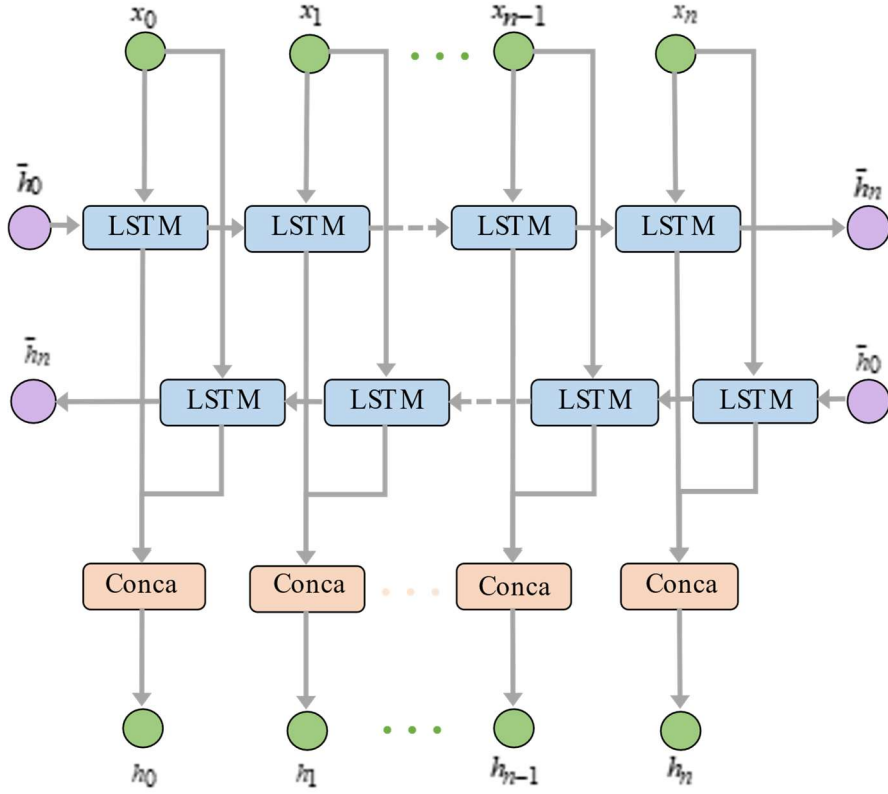


FIGURE 2 The structure of BLSTM. (Conca is the abbreviation for concatenate.)

The forward LSTM unit captures past information of the input data sequence, and the reverse LSTM unit focuses on future information. The BLSTM combines the hidden layer state \vec{h}_t of the forward LSTM unit and the hidden layer state \overleftarrow{h}_t of the reverse LSTM unit at the time t to have the output H_t , which are represented as follows:

$$\vec{h}_t = \overline{LSTM}(x_t, \vec{h}_{t-1}, \vec{C}_{t-1}) \quad (7)$$

$$\overleftarrow{h}_t = \overleftarrow{LSTM}(x_t, \overleftarrow{h}_{t+1}, \overleftarrow{C}_{t+1}) \quad (8)$$

$$H_t = [\vec{h}_t, \overleftarrow{h}_t] \quad (9)$$

2.3 ET

ET, an integrated learning method, constructs unpruned decision trees in a top-down way, similar to RF, but introduces more randomness and diversity^[29].

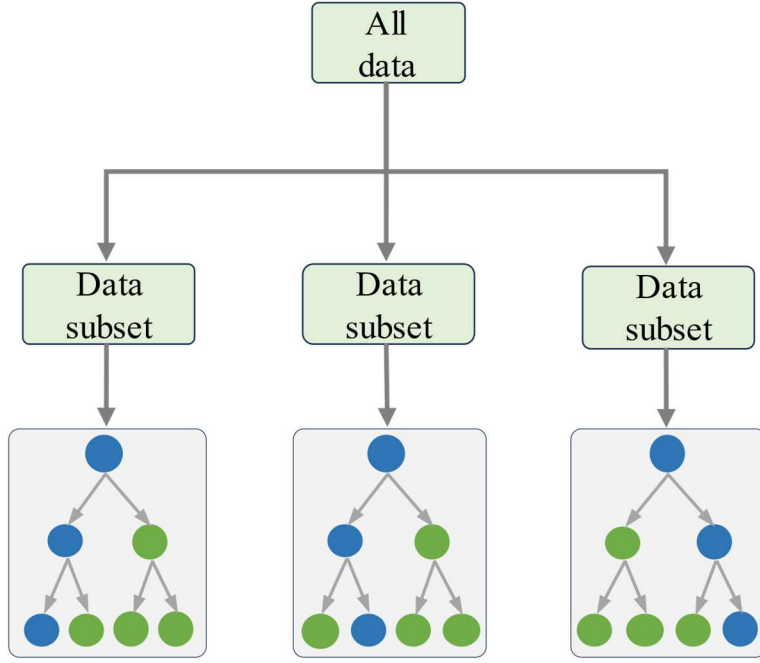


FIGURE 3 The structure of ET.

As shown in Figure 3, ET analyzes the complete raw data when constructing a decision tree. First, a subset of features is randomly selected to train a single decision tree. Second, the feature subset is randomly divided by N feature attributes, and the Gini index for the N divisions is calculated. Finally, the division with the smallest Gini index is chosen for node classification^[30]. The Gini index of the sample set D is denoted as $Gini(D)$, and the Gini index of the subset of D as $Gini_{sub}(D^v)$. These are expressed as follows:

$$Gini(D) = \sum_{v=1}^V \frac{|D^v|}{|D|} Gini_{sub}(D^v) \quad (10)$$

$$Gini_{sub}(D^v) = 1 - \sum_{i=1}^{|y|} (p_i^v)^2 \quad (11)$$

The Gini index quantifies the influence of features on the results, and the smaller the Gini index, the more likely the samples in the node belong to the same class. Therefore, ET selects the division points by calculating the Gini index, which improves the fault diagnosis performance of the model by selecting the divisions favourable to the current node while maintaining the randomness of the tree.

3 PREPARATION FOR TDLN-TREES FAULT DIAGNOSIS

TDLN-trees for fault diagnosis tasks require extracting the corresponding timing features of chemical production data and performing preprocessing operations such as normalization and one-hot encoding. The specific details are as follows:

3.1 Data extraction based on sliding-windows method

In this paper, we use the sliding window method to capture features with temporal correlation. The core concept of the sliding window method involves sliding a window of width w and step size s across the sample set until its end, thereby generating continuous and partially overlapping feature matrices while integrating fault types into label matrices. The features extracted by the sliding window method can help the model to perceive the temporal evolution of data, expressed as follows:

$$M_{F,k} = [f_{k,1}, f_{k,2}, \dots, f_{k, \lfloor \frac{N-w}{s} + 1 \rfloor}] \quad (12)$$

$$M_{L,k} = [l_{k,1}, l_{k,2}, \dots, l_{k, \lfloor \frac{N-w}{s} + 1 \rfloor}] \quad (13)$$

where $M_{F,k}$ and $M_{L,k}$ represent the feature and label matrix windows of the k_{th} sample set respectively, $\lfloor \frac{N-w}{s} + 1 \rfloor$ is the largest integer not exceeding $\frac{N-w}{s} + 1$, and N is the size of sample set, requiring k to be greater than w . In the diagnostic stage, if N is less than w , then $M_{F,k}$ consists of all the feature vectors of the k_{th} sample set. The same applies to $M_{L,k}$.

The values of w and s must be finely tuned through experimental validation. The choice of w should consider the temporal correlation and avoid introducing extraneous historical data, thereby lessening the computational load of model. Similarly, selecting s should strike a balance between preserving adequate information and minimizing redundancy. Properly selected w and s can ensure the data features contain both the dynamic and static aspects of the chemical production process, facilitating subsequent processing.

3.2 Data normalization using data from normal operating state

Data features extracted using the sliding window method vary significantly across physical units and value ranges, necessitating to be normalized. This ensures a consistent scale for each feature type and balances the learning of model across all features.

3.3 One-hot encoding for sample data labels

To adapt the sample labels for the input of model, we apply one-hot encoding to the label matrix generated by the sliding window method. Specifically: for a sample with n categories, each category is mapped to an n -dimensional binary vector, collectively forming a matrix.. It can eliminate the ordinal relationship between labels, enabling the model to more effectively understand and process the fault information of sample. One-hot coding is expressed as follows:

$$Encoding_j = [0, 0, \dots, i, \dots, 0] \quad (14)$$

where j denotes the j_{th} sample, i represents the i_{th} labeling category ($0 \leq i \leq n$), and all positions are 0 except for the i_{th} element, which is 1.

4 TDLN-TREES FAULT DIAGNOSIS

This section describes in detail the structure of TDLN-trees and the process of TDLN-trees for fault diagnosis in real chemical production.

4.1 Establishment of the TDLN-trees

Addressing the issues of high complexity and challenging fault diagnosis in the chemical production process, this subsection proposes a new fault diagnosis model named TDLN-trees.

Its structure is shown in Figure 4. The specific details are as follows:

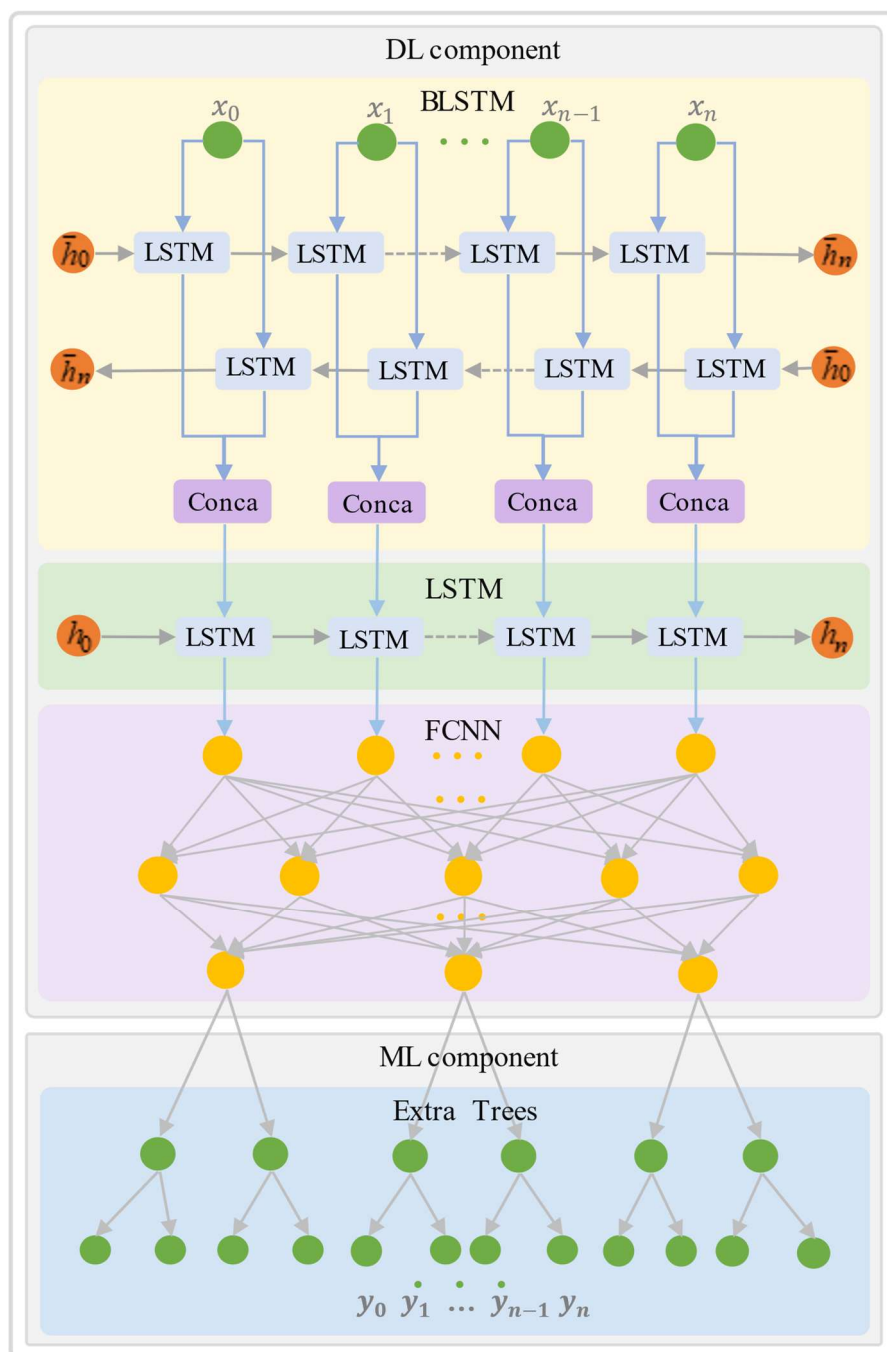


FIGURE 4 The structure of TDLN-trees.

Given the continuous nature of chemical production, process variables fall within the time series category. The BLSTM layer, constituting the first key part of TDLN-trees, is introduced initially. The addition of the BLSTM layer allows the model to capture the forward and backward temporal dynamics of industrial process variable data, its output is represented by Equation (9). Subsequently, the output of the BLSTM layer is fed into the LSTM layer, which is the second key part of TDLN-trees. This LSTM layer further improves the capacity of model to capture short-term dependencies in process variable data, with its output in Equation (6). Next, the output of the LSTM layer is relayed to the FCNN layer, the third key part of TDLN-trees. The FCNN layer can combine and transform temporal features to enhance the ability of TDLN-trees to interpret higher-level data. Its output is as follows:

$$\partial = \sigma (W * x + b) \quad (15)$$

where x represents the input features, W represents the weight matrix, b is the bias, and σ is the activation function 'SELU'.

The BLSTM layer, LSTM layer, and FCNN layer collaboratively process the complex temporal data, constituting the deep learning component. Cross-entropy loss evaluates the fault diagnosis capability of the deep learning component. It indicates the discrepancy between the probability distributions of the model's output and the actual labels. And we adjust the component parameters to minimize the cross-entropy loss and improve the fault detection rate of TDLN-trees.

Next is the introduction of ET, ET belongs to the machine learning component of TDLN-trees. The FCNN layer output is passed to ET, which selects division points using the Gini index (Equation (11)) and maps process variable features to corresponding fault types. Therefore, through the above steps, TDLN-trees can improve the accuracy of fault diagnosis and reduce the occurrence of false alarms and omissions to ensure the stability and safety of chemical system operations.

4.2 TDLN-trees fault diagnosis process

This section explains the application of TDLN-trees in fault diagnosis within real chemical production. As shown in Figure 5, the fault diagnosis comprises two parts: offline fault learning stage and online fault diagnosis stage.

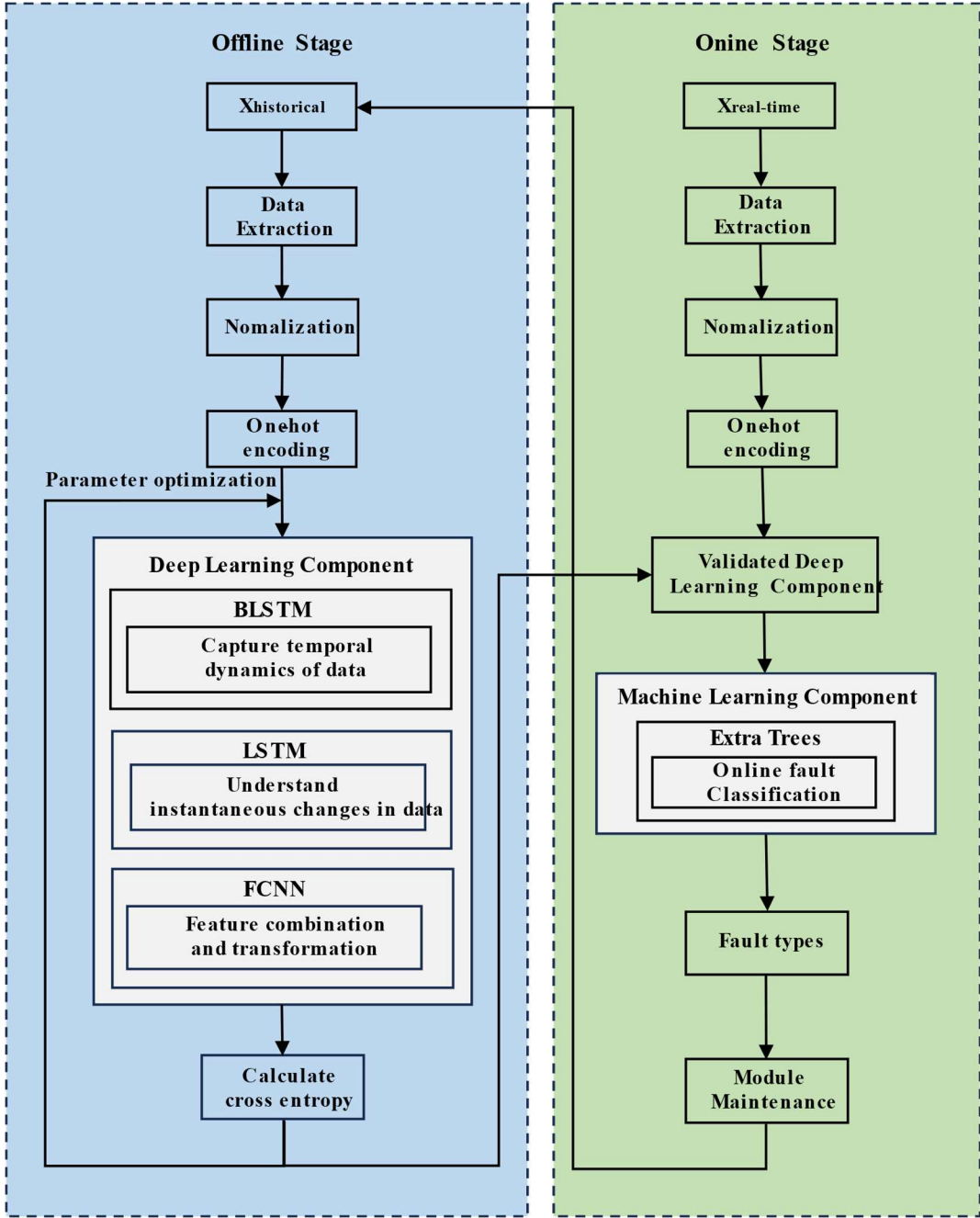


FIGURE 5 TDLN-trees fault diagnosis process.

Offline fault learning stage: As shown in Figure 6. First, the offline time series data are processed using the sliding window method to generate the feature matrices and label matrices with temporal correlation. Second, the matrices are preprocessed, involving normalization of

fault data using normal operation state data and one-hot encoding of label matrices, both serving as model's input sequences. Subsequently, the preprocessed matrices are split into training set and testing set. The DL Component, trained on the training set, calculates cross-entropy loss for performance evaluation and parameter adjustment. Finally, the testing set is fed into the trained TDLN-trees, processed by the DL Component and ML Component, and we fine-tune the parameters of the DL Component according to the processing results. The operations mentioned above ensure that TLDN-trees can realize fault diagnosis perfectly.

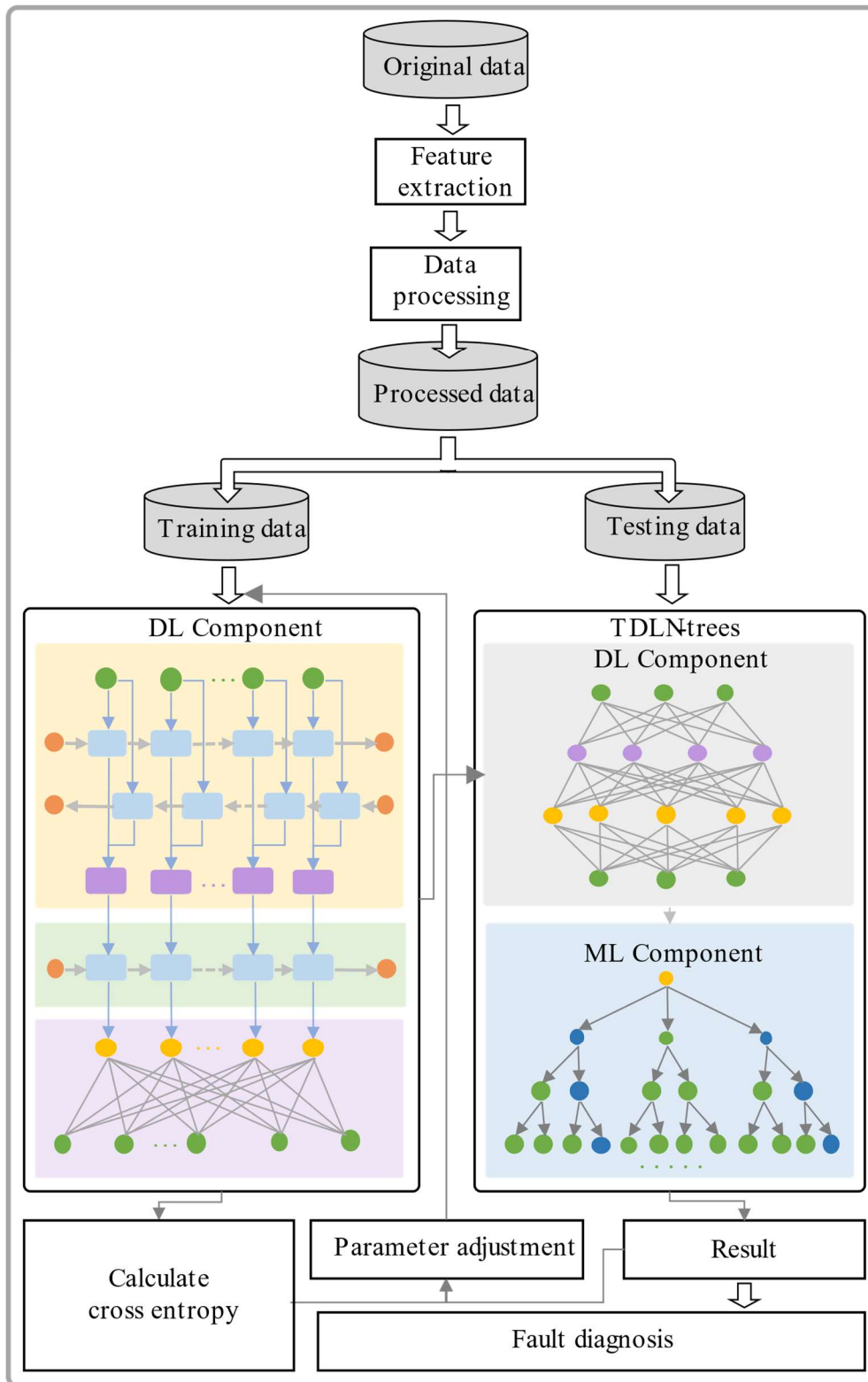


FIGURE 6 TDLN-trees offline training process. (DL, ML is the abbreviation for deep learning and machine learning.)

Online fault diagnosis stage: As shown in Figure 5. First, online monitoring data from chemical production are processed using the sliding window method, normalization, and one-

hot encoding, similar to the preprocessing method of the offline stage; Second, the processed data are input into the trained and parameter-optimized DL Component; After that, ET realizes the classification, which determine the fault types of the monitoring data by comparing the Gini index. The final step in online diagnosis involves enriching the dataset by incorporating fault-detected monitoring data into the historical database.

5 EXPERIMENT

To validate the fault diagnosis performance of TDLN-trees, we conduct various experiments based on the Tennessee Eastman Process (TEP) dataset, and select accuracy, Precision-Recall (PR) curves, and Receiver Operating Characteristic (ROC) curves as indicators to assess the fault diagnosis performance.

5.1 Tennessee Eastman Process

TEP is a complex model for simulating chemical processes, and is often utilized to test the effectiveness of process monitoring and fault diagnosis methods^[31]. As shown in Figure 7, the TEP model comprises five operating units: Stripping Column, Condenser, Compressor, Reactor, and Separator. For detailed roles of these operating units, refer to references [32,33]. A series of chemical reactions were carried out in these operating units, where the gas-phase reactants A, C, D, and E are converted to liquid-phase products G and H, generating by-products F, and B is an inert ingredient not participating in the chemical reaction. For the specific chemical reaction process, refer to reference [34].

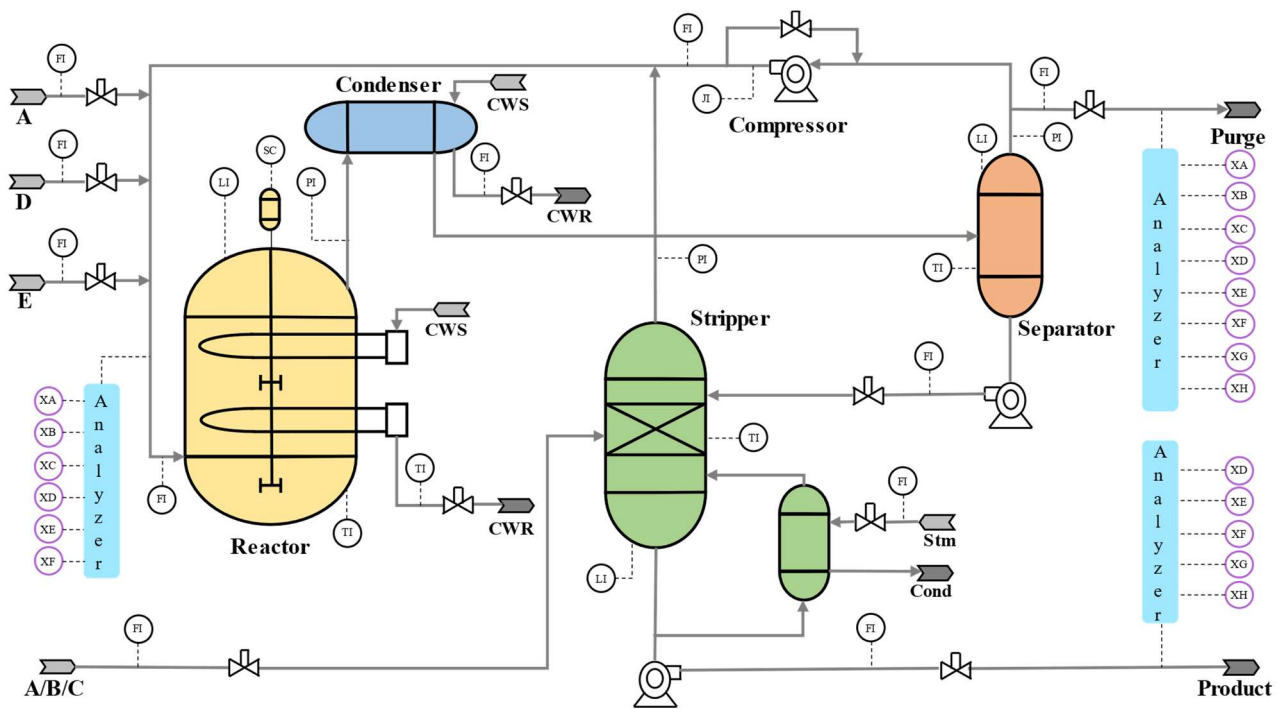


FIGURE 7 The process diagram of TEP.

TEP can simulate the normal operating state and 20 fault states of the chemical process. It contains 11 manipulated variables and 41 measurement variables, and gathering these 52 variables reflects to the operational state of the system^[35]. As shown in Table 1, 0 represents the normal operating state, and 1 to 20 represents the different types of fault states. Since the mean and variance parameters show significant variations in fault types 3, 9, and 15, we exclude these three fault types for further analysis and evaluation.

TABLE1 TEP process disturbances table.

Fault ID	Fault description	Fault Type
1	A/C feed ratio, B composition constant (stream 4)	Step
2	B composition, A/C ratio constant (stream 4)	Step
3	D feed temperature (stream 2)	Step
4	Reactor cooling water inlet temperature	Step
5	Condenser cooling water inlet temperature	Step
6	A feed loss (stream 1)	Step
7	C header pressure loss - reduced availability (stream 4)	Step
8	A, B, C feed composition (stream 4)	Random variation
9	D feed temperature (stream 2)	Random variation
10	C feed temperature (stream 4)	Random variation
11	Reactor cooling water inlet temperature	Random variation
12	Condenser cooling water inlet temperature	Random variation
13	Reaction kinetics	Slow drift
14	Reactor cooling water valve	Sticking
15	Condenser cooling water valve	Sticking
16	Unknown	Random variation
17	Unknown	Random variation
18	Unknown	Random variation
19	Unknown	Sticking
20	Unknown	Random variation

5.2 Parameter Setup

The parameter settings for each subnetwork layer of TDLN-trees are shown in Table 2. Taking the input layer as an example, 'None' represents the batch size of TDLN-trees, specified by the training parameter 'batch size', while 20 and 52 represent the time step and the number of features, respectively. The activation function of BLSTM and LSTM layers is 'tanh', which helps to attenuate the gradient drift. FCNN is a two-layer structure, and its activation function is 'SELU', which can help the model self-normalize. In the training stage, set 'epochs' as 50, 'batch size' as 256, optimizer as 'adam', and utilize the adaptive learning rate optimization algorithm. Finally, we verify the effect of different sliding window widths w and step size s on the accuracy and runtime. The experimental results are shown in Table 3, $w=30$ and $s=20$ are set to achieve better diagnostic results and maintain a smaller computational load.

TABLE 2 The parameters of TDLN-trees subnetwork layers.

Layers	Section	Architecture/Parameters
Input	DL Component	None \times 20 \times 52
BLSTM	DL Component	None \times 20 \times 256
LSTM	DL Component	None \times 128
FCNN	DL Component	None \times 300 - None \times 18
Extra Trees	ML Component	n_estimators=112 max_depth=31

TABLE 3 The impact of different values of w and s on training effects

w	s	Accuracy(%)	Time(s)
35	15	99.12	598.54
35	20	99.12	515.08
30	10	99.11	675.28
30	20	99.07	339.57
30	25	98.91	321.11
25	10	98.63	637.36
25	20	98.49	335.13
20	5	98.15	901.97
20	10	97.95	621.15

5.3 Experimental Results and Analysis

5.3.1 Accuracy and loss curves

As shown in Figure 8 is the accuracy and loss curves for the training and testing set, the red line and purple line in Figure 8A represent the accuracy of the training and testing set, respectively, while the blue and green line in Figure 8B represent their cross-entropy loss. In the first 12 epochs of 50 epochs, the accuracy of the training and testing set continues to increase, reaches stability at the 20th epoch, and then slightly fluctuates. The accuracy of the testing set can stably exceed 95%, with the highest accuracy reaching 99.07%, corresponding to a loss of 0.0225. These results demonstrate the feasibility of TDLN-trees.

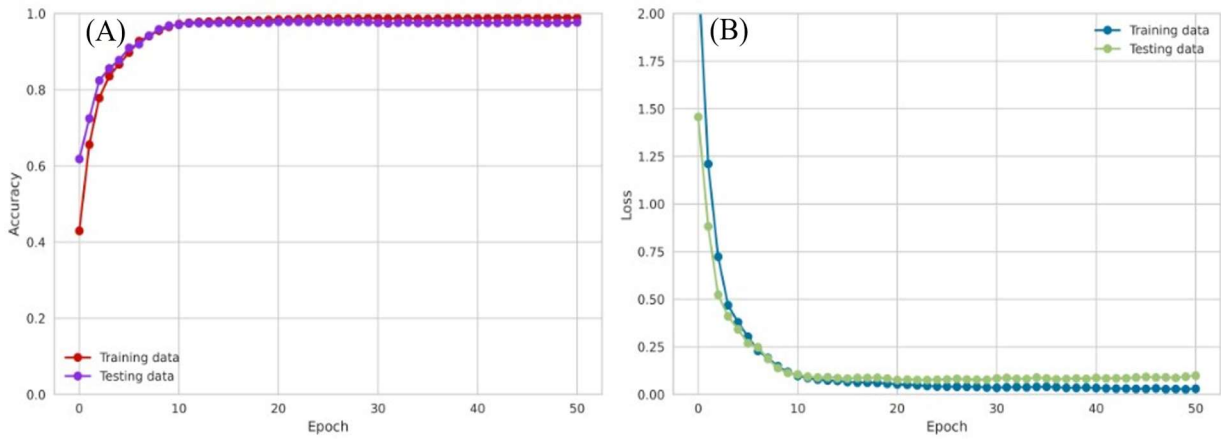


FIGURE 8 (A) Training accuracy and testing accuracy, (B) Training loss and testing loss.

5.3.2 Analysis of fault diagnosis results

Figure 9 shows the confusion matrix for TDLN-trees fault diagnosis, its rows represent the predicted types, and columns represent the actual types. The main diagonal represents the accuracy of classifying corresponding fault types, while other values show misclassification proportions. The darker colour in the matrix represents the higher classification accuracy. Analysis of Figure 9 reveals that diagonal elements are predominantly close to 1, while off-diagonal elements are near 0. The average diagnostic accuracy of TDLN-trees across the normal state and 17 fault states reaches 97.81%. These results demonstrate the excellent performance of TDLN-trees in fault diagnosis and prove the superiority of TDLN-trees.

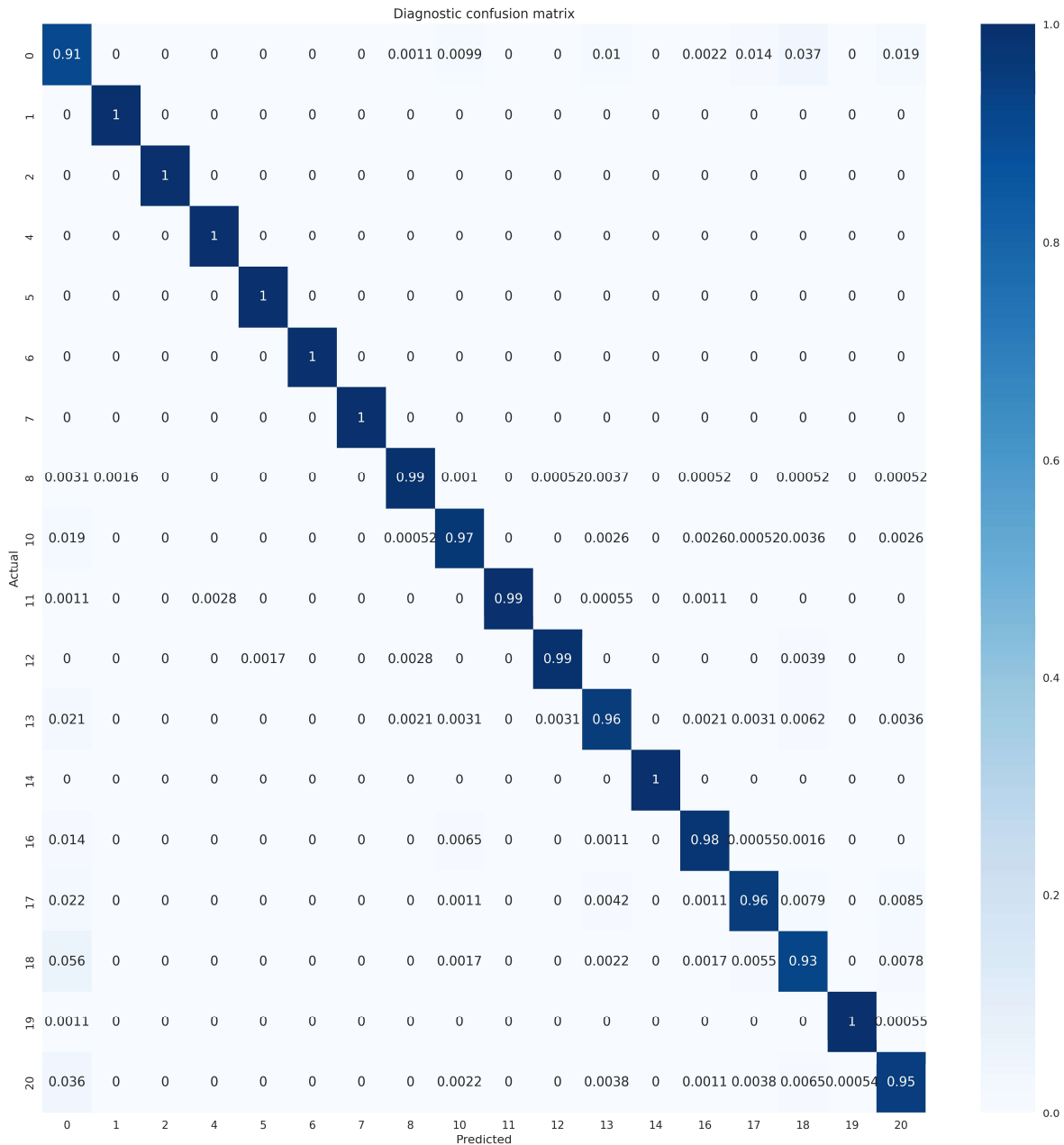


FIGURE 9 Confusion matrix of fault diagnosis for TDLN- trees.

5.3.3 Precision-recall curves and receiver operating characteristic curves

The PR curves, with the vertical axis representing precision and the horizontal axis denoting recall, illustrate the performance trends of TDLN-trees under various classification thresholds. The closer the Area Under Curve (AUC) is to 1.00 indicates that the more samples of TDLN-trees are correctly fault diagnosed. As shown in Figure 10, the PR curves for the normal operation state and 17 fault types all converge towards the upper right of the figure, with the AUC of each curve exceeding 0.91, and many reaching 1.00. These results reflect the

high precision and recall of TDLN-trees in fault diagnosis, and confirm the effectiveness of TDLN-trees.

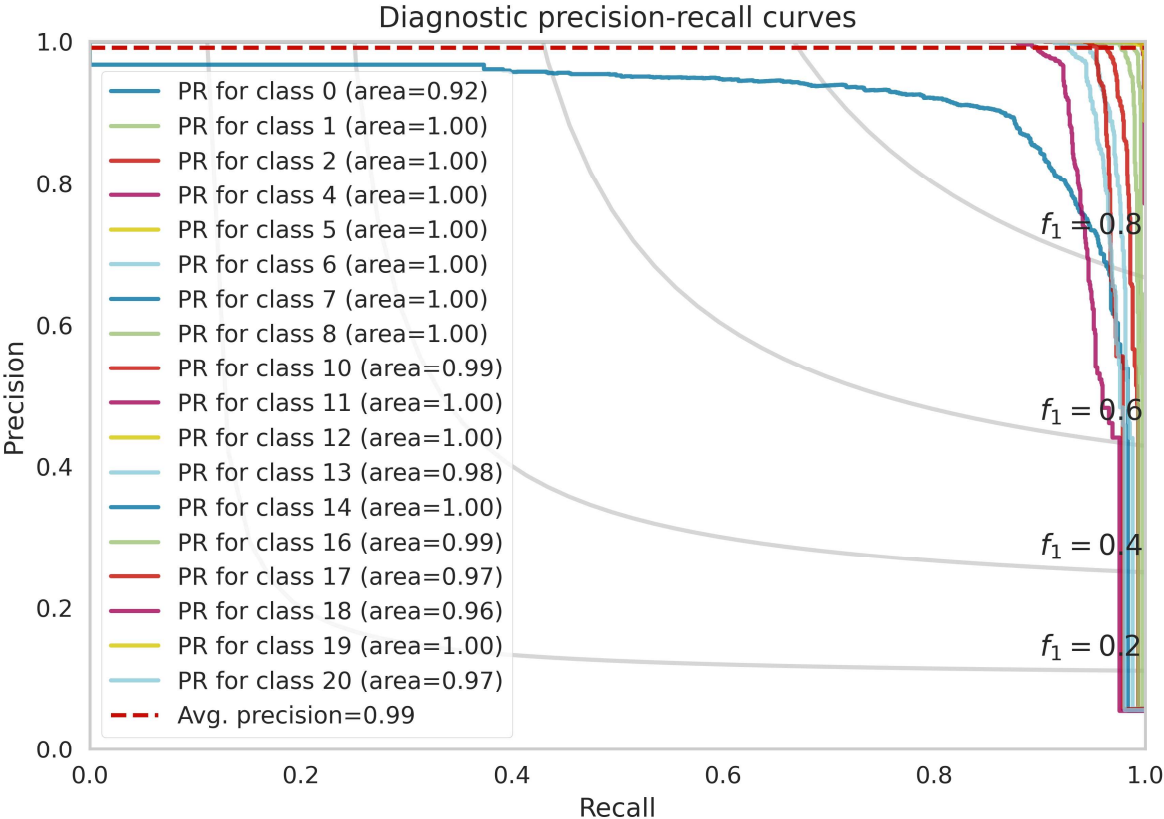


FIGURE 10 Precision-recall curves of fault diagnosis for TDLN-trees.

The ROC curves, with the vertical axis representing the true-positive rate and the horizontal axis denoting the false-positive rate, show the trend of the true-positive rate and false-positive rate of TDLN-trees across various classification thresholds. The evaluation metric AUC for the ROC curves, similar to that for the PR curves, indicates that the closer it is to 1, the better the TDLN-trees perform in fault diagnosis. As shown in Figure 11, the ROC curves for the normal operation state and the 17 fault states all tend to converge to the upper left of the figure, with all AUCs being at least 0.96, while the micro and macro ROC curves have AUCs of 0.99. These results demonstrate that TDLN-trees can maintain a high fault diagnostic rate while reducing the false-positive rate for different fault types.

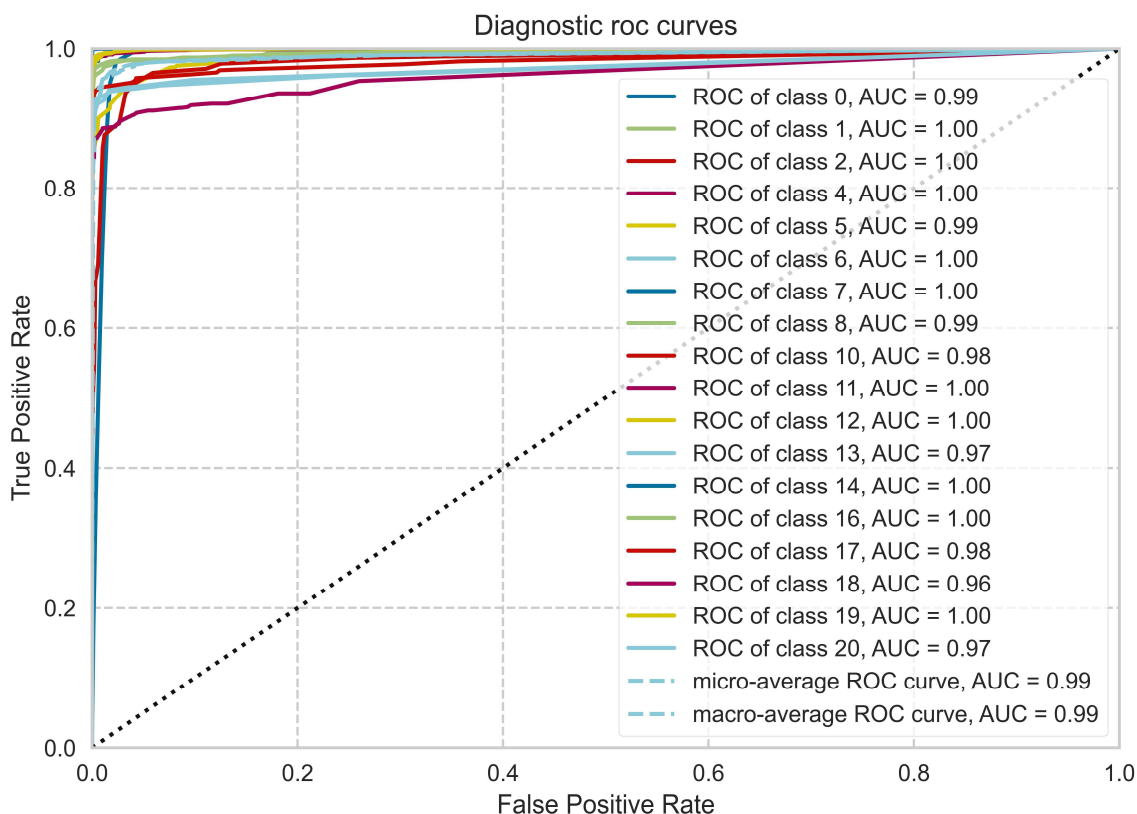


FIGURE 11 Roc curves of fault diagnosis for TDLN-trees.

5.4 Comparison with other state-of-the-art methods

We compare TDLN-trees with other state-of-the-art methods for fault diagnosis, and experimentally validate them on TEP. As shown in Table 4, the Fault Diagnosis Rate (FDR) of TDLN-trees is 98.24%, which is higher than that of other methods, and its FDRs for faults 1, 2, 4, 5, 6, 7, and 14 are 100%. The FDR of DSAE^[36] is 88.34%, as DSAE overly focuses on identifying fault states, resulting in high complexity. TceOne^[37] records an FDR below 53% for faults 5 and 16, due to its One-class classifier approach that relies on features from normal state data, hindering its ability to handle fault states that are not markedly different from normal states or are highly variable. CRAE^[38] has an FDR below 81% for faults 16 and 18, as it struggles to effectively push the decision boundary with some faults. OI DCNN^[39] has an FDR below 84% for faults 4 and 19, with a 55.4% FDR for fault 16, due to its proficiency in processing structured data like images, leading to degraded performance with unstructured data. DHSF-DBN^[40] has an FDR 0.54% lower than TDLN-trees, and Target Transformer^[41] has an FDR of 94.45%, neither matching TDLN-trees in adapting to complex chemical production data. TVAE^[42] has an FDR of 2.26% lower than TDLN-trees, as it loses some original data

details when compressing data into a low-dimensional space, ignoring small key features. This comparison experiment confirms the robustness and superiority of TDLN-trees among different faults.

TABLE 4 The FDRs of TDLN-trees and other state-of-the-art methods for TEP.

Fault	DSAE	TeeOne	CRAE	OIDCNN	DHSF-DBN	Target Transformer	TVAE	Propose method
1	99.30	99.80	100.00	100.00	99.88	99.75	98.70	100.00
2	96.80	98.90	97.40	98.70	99.50	98.44	98.40	100.00
4	100.00	100.00	100.00	83.50	100.00	99.62	100.00	100.00
5	95.60	41.50	99.57	93.30	100.00	91.88	97.10	100.00
6	100.00	100.00	100.00	95.50	100.00	98.21	99.30	100.00
7	100.00	100.00	100.00	96.10	100.00	99.94	100.00	100.00
8	87.00	97.40	84.38	95.90	99.62	95.56	97.30	98.85
10	68.30	97.00	83.30	95.60	88.75	97.69	96.50	96.86
11	81.30	98.00	96.96	94.50	93.38	98.06	85.50	99.45
12	94.10	89.80	90.89	90.70	99.75	97.06	95.90	99.16
13	78.10	98.00	88.07	96.90	96.75	96.12	97.10	95.57
14	99.60	99.80	100.00	100.00	100.00	98.75	99.20	100.00
16	86.00	52.50	78.96	55.40	97.87	52.69	93.30	97.63
17	79.80	98.60	95.44	93.90	98.87	94.75	90.10	95.52
18	90.60	93.30	80.48	89.50	90.00	94.25	98.30	92.51
19	66.60	98.70	99.78	82.20	99.75	98.69	92.80	99.84
20	78.60	96.00	90.89	96.40	97.87	94.25	92.20	94.61
Average	88.34	91.72	93.30	91.65	97.76	94.45	95.98	98.24

5.5 Ablation experiment

We remove the deep learning component and the machine learning component from the TDLN-trees framework sequentially to assess their contributions, the experimental results are shown in Table 5. Compared to TDLN-tree, the FDR is reduced by 6.11% and 0.48% when the deep learning component and the machine learning component are removed, respectively, indicating that both components can improve the fault diagnosis performance of TDLN-trees, the details described as follows:

Deep Learning Component: as shown in Table 5, the fault diagnosis performance is worse when the deep learning component is removed, particularly for faults 10, 11, 16, and 20, with FDR reductions of 11.21%, 20.19%, 14.96%, and 20.8%, respectively. The component can handle the complex patterns and correlations in time series data, capture long and short-term dependencies, and refine and enhance feature representations. Thus, adding the deep learning component to the TDLN-trees framework results in better fault diagnosis performance than without the component.

Machine Learning Component: as shown in Table 5, the FDRs for faults 8 and 10 of TDLN-trees are reduced by 2.5% and 3.48%, respectively, when the machine learning component is removed. The component integrates multiple decision trees, classifying features extracted by the deep learning component using the Gini index, thereby enhancing the generalization ability of TDLN-trees across various fault types. Therefore, incorporating the machine learning component into the TDLN-trees framework can improve the FDR of TDLN-trees.

In summary, both the deep learning and machine learning components are crucial for enhancing the fault diagnosis performance of TDLN-trees, with their combination offering the most significant improvement in real chemical production.

Table 5 The FDRs of TDLN-trees in ablation experiment.

Fault	Without DL component	Δ	Without ML component	Δ	Propose method
1	99.07	-0.93	100.0	0	100.00
2	97.17	-2.83	100.0	0	100.00
4	99.78	-0.22	98.30	-1.7	100.00
5	98.55	-1.45	100.00	0	100.00
6	100.00	0	100.00	0	100.00
7	100.00	0	100.00	0	100.00
8	96.06	-2.79	96.35	-2.5	98.85
10	85.65	-11.21	93.38	-3.48	96.86
11	79.26	-20.19	99.78	0.33	99.45
12	96.09	-3.07	98.84	-0.32	99.16
13	89.79	-5.78	95.43	-0.14	95.57
14	96.58	-3.42	100.00	0	100.00
16	82.67	-14.96	96.39	-1.24	97.63
17	89.68	-5.84	95.49	-0.03	95.52
18	91.18	-1.33	92.94	0.43	92.51
19	90.76	-9.08	99.77	-0.07	99.84
20	73.81	-20.8	95.18	0.57	94.61
Average	92.12	-6.11	97.76	-0.48	98.24

6 CONCLUSION

In this paper, a new fault diagnosis model named TDLN-trees is proposed for the chemical production process. It integrates the strengths of deep learning and machine learning techniques, and combines the advantages of BLSTM, LSTM, FCNN, and ET. First, the BLSTM layer in the deep learning component comprehensively analyzes the dynamic characteristics of time series data, the LSTM layer precisely identifies and captures the instantaneous changes in the

data, while the FCNN layer enhances the understanding of higher-level data. Second, the ET in the machine learning component calculates the Gini index for node segmentation and realizes fault classification. In the experimental demonstration based on TEP, TDLN-trees was compared with other state-of-the-art methods and demonstrated superior performance, achieving a 98.24% FDR, surpassing that of the other methods. Ablation experiments also confirm the effectiveness of the proposed method for fault diagnosis in chemical production.

ACKNOWLEDGEMENTS

This work is supported by the National Natural Science Foundation of China (62203164, 62373144), Scientific Research Fund of Hunan Provincial Education Department (Outstanding Young Project) (21B0499), Hunan Provincial Department of Education (Project No. 22A0349).

REFERENCES

- [1] M. Sajid, J. Płotka-Wasyłka, *Talanta*. **2022**, 238, 123046.
- [2] X. Bi, R. Qin, D. Wu, S. Zheng, J. Zhao, *Comput. Chem. Eng.* **2022**, 164, 107884.
- [3] V. Hessel, N. N. Tran, M. R. Asrami, Q. D. Tran, N. V. D. Long, M. Escrivà-Gelonch, J. O. Tejada, S. Linke, K. Sundmacher, *Green Chem.* **2022**, 24(2): 410-437.
- [4] M. T. Amin, S. Imtiaz, F. Khan, *Chem. Eng. Sci.* **2018**, 189: 191-211.
- [5] L. Ming, J. S. Zhao, *International Symposium on Advanced Control of Industrial Processes* IEEE. Taipei, China, May **2017**.
- [6] K. Zhang, B. Jiang, P. Shi, *IET Control Theory & Applications*. **2009**, 3(2): 189-199.
- [7] P. Li, V. Kadiramanathan, *IEEE Trans. Syst. Man Cybern. Part C Appl. Rev.* **2001**, 31(3): 337-343.
- [8] M. Dong, C. Liu, G. Y. Li, *IEEE Trans. Control Syst. Technol.* **2010**, 18(2): 510-515.
- [9] P. Jieyang, A. Kimmig, W. Dongkun, Z. Niu, F. Zhi, W. Jiahai, X. Liu, J. Ovtcharova, J. *Intell. Manuf.* **2023**, 34(8): 3277-3304.
- [10] N. Nor. Md, R. C. Hassan. Che, A. M. Hussain, *Rev. Chem. Eng.* **2020**, 36(4): 513-553.
- [11] R. Dunia, S. J. Qin, T. F. Edgar, T. J. McAvoy, *AIChE J.* **1996**, 42(10): 2797-2812.
- [12] C. Botre, M. Mansouri, M. Nounou, H. Nounou, N. M. Karim, *J. Loss Prev. Process Ind.* **2016**, 43: 212-224.

- [13] B. Schölkopf, A. Smola, K. R. Müller, *Neural Comput.* **1998**, 10(5): 1299-1319.
- [14] M. Meuwly, *Chem. Rev.* **2021**, 121(16): 10218-10239.
- [15] S. Mahadevan, S. L. Shah, *J. Process. Contr.* **2009**, 19(10): 1627-1639.
- [16] A. Roy, S. Chakraborty, *Reliab. Eng. Syst. Saf.* **2023**: 109126.
- [17] P. eurts, D. Ernst, L. Wehenkel, *Mach. Learn.* **2006**, 63: 3-42.
- [18] M. Arya, G. H. Sastry, A. Motwani, S. Kumar, A. Zaguia, *Front. Public Health*, **2022**, 9: 797877.
- [19] Y. Sina, Y. Shen, A. M. Gibran, *IEEE Open J. Ind. Electron. Soc.* **2023**.
- [20] Y. Lei, B. Yang, X. Jiang, F. Jia, N. Li, A. K. Nandi, *Mech. Syst. Signal Process.* **2020**, 138: 106587.
- [21] Z. Ren, W. Zhang, Z. Zhang, *IEEE Trans. Ind. Inf.* **2019**, 16(8): 5042-5052.
- [22] L. Wen, X. Li, L. Gao, Y. Zhang, *IEEE Trans. Ind. Electron.* **2017**, 65(7): 5990-5998.
- [23] S. S. Roy, S. Chatterjee, S. Roy, P. Bamane, A. Paramane, U. M. Rao, M. T. Nazir, *IEEE Trans. Ind. Appl.* **2022**, 58(4): 4542-4551.
- [24] S. Zhang, T. Qiu, *Chem. Eng. Sci.* **2022**, 251: 117467.
- [25] Y. Han, N. Ding, Z. Geng, Z. Wang, C. Chu, *J. Process Control.* **2020**, 92: 161-168.
- [26] D. E. Rumelhart, G. E. Hinton, R. J. Williams, *nature.* **1986**, 323(6088): 533-536.
- [27] A. Sherstinsky, *Phys. D.* **2020**, 404: 132306.
- [28] G. Van Houdt, C. Mosquera, G. Nápoles, *Artif. Intell. Rev.* **2020**, 53: 5929-5955.
- [29] M.W. Ahmad, J. Reynolds, Y. Rezgui, *J. Cleaner Prod.* **2018**, 203: 810-821.
- [30] Q. W. Wu, R. F. Cao, J. F. Xia, J. C. Ni, C. H. Zheng, Y. S. Su, *IEEE/ACM Trans. Comput. Biol. Bioinf.* **2021**, 19(6): 3171-3178.
- [31] H. Pu, J. Liu, Z. Chen, X. Yang, C. Ren, Z. Xu, Y. Jian, *International Conference on Computing, Control and Industrial Engineering. Singapore, February* **2023**.
- [32] N. L. Ricker, *J. Process Control.* **1996**, 6(4): 205-221.
- [33] I. Lomov, M. Lyubimov, I. Makarov, L. E. Zhukov, *J. Ind. Inf. Integr.* **2021**, 23: 100216.
- [34] P. R. Lyman, C. Georgakis, *Comput. Chem. Eng.* **1995**, 19(3): 321-331.
- [35] L. Zhang, Z. Song, Q. Zhang, Z. Peng, *Neural Comput. Appl.* **2022**, 34(11): 8575-8585.
- [36] P. Peng, Y. Zhang, H. Wang, H. Zhang, *ISA Trans.* **2022**, 125: 371-383.
- [37] S. Wang, Q. Zhao, Y. Han, J. Wang, *IEEE Trans. Instrum. Meas.* **2023**.

- [38] Y. Ma, H. Shi, S. Tan, Y. Tao, B. Song, *IEEE Trans. Instrum. Meas.* **2022**, 71: 1-15.
- [39] M. Li, P. Peng, H. Sun, M. Wang, H. Wang, *IEEE Trans. Autom. Sci. Eng.* **2023**.
- [40] B. Liu, Y. Chai, Y. Liu, C. Huang, Y. Wang, Q. Tang, *J. Process Control.* **2021**, 102: 54-65.
- [41] Z. Wei, X. Ji, L. Zhou, Y. Dang, Y. Dai, *Process Saf. Environ. Prot.* **2022**, 167: 480-492.
- [42] L. Qi, Y. Ren, Y. Fang, J. Zhou, *Neural Comput. Appl.* **2023**, 35(29): 22007-22026.